



Article

Effect of Non-Identical Magnetic Fields on Thermomagnetic Convective Flow of a Nanoliquid Using Buongiorno's Model

Nidhal Ben Khedher ^{1,2}, Mikhail Sheremet ^{3,*}, Abed Saif Alghawli ⁴, Abdullah Mohamed ⁵ and Seyed Abdollah Mansouri Mehryan ^{6,*}

- ¹ Department of Mechanical Engineering, College of Engineering, University of Ha'il, Ha'il 81451, Saudi Arabia; n.khedher@uoh.edu.sa
² Laboratory of Thermal and Energetic Systems Studies (LESTE), National School of Engineering of Monastir, University of Monastir, Monastir 5000, Tunisia
³ Laboratory on Convective Heat and Mass Transfer, Tomsk State University, 634045 Tomsk, Russia
⁴ Computer Science Department, Prince Sattam Bin Abdulaziz University, AL-Aflaj 11912, Saudi Arabia; a.alghawly@psau.edu.sa
⁵ Research Centre, Future University in Egypt, New Cairo 11745, Egypt; mohamed.a@fue.edu.eg
⁶ Young Researchers and Elite Club, Yasooj Branch, Islamic Azad University, Yasooj 7591493686, Iran
* Correspondence: michael-sher@yandex.ru (M.S.); s_mansourimehryan@sbu.ac.ir or alal171366244@gmail.com (S.A.M.M.)

Abstract: Energy transport intensification is a major challenge in various technical applications including heat exchangers, solar collectors, electronics, and others. Simultaneously, the control of energy transport and liquid motion allows one to predict the development of the thermal process. The present work deals with the computational investigation of nanoliquid thermogravitational energy transport in a square region with hot cylinders along walls under non-uniform magnetic influences. Two current-carrying wires as non-identical magnetic sources are set in the centers of two heated half-cylinders mounted on the bottom and left borders, while the upper wall is kept at a constant low temperature. Buongiorno's model was employed with the impact of Brownian diffusion and thermophoresis. Governing equations considering magnetohydrodynamic and ferrohydrodynamic theories were solved by the finite element technique. The effects of the magnetic sources strengths ratio, Lewis number, Hartmann number, magnetic number, buoyancy ratio, Brownian motion characteristic, and thermophoresis feature on circulation structures and heat transport performance were examined. For growth of magnetism number between 0 and 10^3 one can find an increment of heat transfer rate for the half-cylinder mounted on the bottom wall and a reduction of heat transfer rate for the half-cylinder mounted on the left wall, while for an increase in magnetism number between 10^3 and 10^4 , the opposite effects occur. Moreover, a rise in the Lewis number characterizes the energy transport degradation. Additionally, an intensification of energy transport could be achieved by a reduction of the thermophoresis parameter, while the Brownian diffusion factor and buoyancy ratio have a negligible influence on energy transport. Furthermore, the heat transfer rate through the half-cylinder mounted on the bottom wall declines with an increase in the magnetic sources strengths ratio.

Keywords: thermogravitational energy; current-carrying wires; non-uniform magnetic force; nanoliquid; Brownian diffusion; thermophoresis

MSC: 76W05; 60J70



Citation: Khedher, N.B.; Sheremet, M.; Saif Alghawli, A.; Mohamed, A.; Mehryan, S.A.M. Effect of Non-Identical Magnetic Fields on Thermomagnetic Convective Flow of a Nanoliquid Using Buongiorno's Model. *Mathematics* **2022**, *10*, 1222. <https://doi.org/10.3390/math10081222>

Academic Editor: Ali Farajpour

Received: 19 February 2022

Accepted: 30 March 2022

Published: 8 April 2022

Publisher's Note: MDPI stays neutral with regard to jurisdictional claims in published maps and institutional affiliations.



Copyright: © 2022 by the authors. Licensee MDPI, Basel, Switzerland. This article is an open access article distributed under the terms and conditions of the Creative Commons Attribution (CC BY) license (<https://creativecommons.org/licenses/by/4.0/>).

1. Introduction

Development of industry demands the control of liquid circulation and energy transport within engineering devices. Nowadays, for this purpose, it is possible to employ nanoliquids that present heat transfer agents (water, oil and ethylene glycol) containing a low concentration of solid nano-sized particles (alumina, copper, copper oxide, and ferric

oxide) [1]. Izadi et al. [2] investigated the convection heat transfer characteristics of nano-suspension flowing in an annulus using the single-phase method. They concluded that the flow characteristics are directly affected by the secondary flow and the axial component of the buoyancy forces. Additionally, the convective heat transfer coefficient alters with a variation of the Richardson number. Selimefendigil and Öztop [3] analyzed the natural heat exchange of carbon nanotube/water nanofluid inside a 3D enclosure. The results indicated a significant enhancement in the thermal index at the highest loading of the nanoparticle. Moreover, various aspects of natural convection heat transfer in enclosures such as heatsinks [4], nano-enhanced heat transfer [5], heat exchangers [6], heat transfer in porous media [7] and thermal energy storage [8] have been investigated in recent works.

Treatment of Darcy-Forchheimer flow of a nanofluid has been investigated under a rotating disk by Hayat et al. [9,10]. Hayat et al. [10] reported a numerical study on the 3D flow of a nanofluid over a nonlinearly stretching sheet. Moreover, the usage of magnetic force for the electrically conductive liquid allows one to manage the flow process and energy transport. Daneshvar Garmroodi et al. [11] studied magnetohydrodynamic laminar convection of Cu-water nanoliquid in an enclosure, including two rotating cylinders. They advised a vertical arrangement of the cylinders, which attains the maximum heat exchange enhancement. Utilizing CuO/water nanofluid, Selimefendigil and Öztop [12] investigated forced convection of flow over cylinders through a duct exposed to magnetic effects. They considered the possible usage of magnetic effects to enhance the heat transfer due to flow structure.

Shafiq et al. [13] considered the magnetohydrodynamic (MHD) convection of nanofluid flow, including microorganisms. They reported that the inclination angle and magnetic parameter could reduce the velocity profile. A 3D analysis of heat transfer and nanofluid flow on a shrinking surface was performed under magnetic effects by Nayak [14]. The presence of porous material and the magnetic field result in a reduction of heat exchange between shrinking surface and nanofluid.

Non-uniform magnetic effects on natural heat exchange of nanofluid flowing in a porous enclosure were analyzed by Izadi et al. [15]. Their results showed that the average Nusselt number had no dependency on magnetic field at low Rayleigh numbers. Mixed convection inside an enclosure filled by CuO/water nanofluid under the effects of a magnetic field was investigated by Selimefendigil and Öztop [16]. Their results confirmed that as the Hartmann number increases, the rate of heat transfer first decreases and then increases. Hayat et al. [17] scrutinized the MHD flow of a nanofluid with binary chemical reaction and activation energy. They reported that the activation energy influenced the concentration boundary layer thickness.

Additionally, some interesting results about the magnetic impact on convective energy transport can be found in [18,19]. Sheikholeslami et al. [18] numerically studied nanoliquid circulation in a porous channel under the impact of the Lorentz force based on the homogeneous nanoliquid approach by the lattice Boltzmann method. They ascertained that Nu rises with the Hartmann number. Malmir–Chegini and Amanifard [19] computationally investigated laminar nanoliquid circulation in a horizontal tube under the non-uniform magnetic influence. It was revealed that employing the magnetic field enhances energy transport in practice.

Gan Jia Gui et al. [20] conducted experiments on ferrofluid heat transfer performance for forced convective flow in microchannels under the external magnetic impact. It was ascertained that the energy transport intensity reduced with the growth of magnetic strength. Calculations on convective energy transport of ferrofluid in a heat sink with porous fins under the uniform magnetic influence were performed by Bezaatpour and Goharkhah [21].

A single-phase nanoliquid approach, combined with Brownian diffusion effects for thermal conductivity, was studied. Authors found that the magnetic field has an important influence on the energy transfer enhancement at low Reynolds numbers. However, the heat transfer coefficient insignificantly changes for the high values of Reynolds numbers. Zhou et al. [22] calculated by the lattice Boltzmann method and experimentally studied the transverse velocity pulsation impact on the energy transport intensity of magnetorheologi-

cal liquid flow in a microchannel with non-uniform magnetic influence. It was observed experimentally that the energy transport rate increment could be achieved by the impact of the alternating magnetic field.

Asadi et al. [23] computationally studied the laminar forced ferrofluid thermal transmission in a channel with corrugated walls under non-uniform magnetic impact. In their study, the governing equations included the slip velocity and Kelvin force. The authors showed that a strong negative magnetic field gradient augments the heat transfer rate. Experimental examination of magnetic impacts on flow structure and energy transport of ferrofluid in a vertical tube was conducted by Zonouzi et al. [24]. Experiments showed an opportunity to enhance the energy transport of magnetic nanofluid (2 vol% Fe_3O_4) with quadrupole magnets.

Moreover, the growth of the Reynolds number decreases the energy transport coefficient when applying magnetic quadrupole. A numerical analysis of the rotating non-uniform magnetic field on ferrofluid forced convective thermal transmission and motion in a horizontal duct was performed by Fadaei et al. [25]. The authors revealed that the considered rotating magnetic field could change the velocity field, and the Nusselt number has an optimum magnitude in terms of the magnetic intensity and frequency. Gibanov et al. [26] numerically considered the mixed convective energy transference within a lid-driven cavity filled with ferrofluid under a variable magnetic effect. They claimed that heat transfer enhancement is obtained by increasing the magnetic number.

Selimefendigil et al. [27] numerically analyzed forced convection of a nanoliquid inside a channel subject to non-uniform magnetic effects. Another study performed by Mehryan et al. [28] is an investigation of a periodic magnetic effect on entropy generation of natural heat exchange inside an enclosure saturated by a nanofluid. The results indicated that the entropy generation of natural heat exchange with the periodic magnetic effect versus the uniform magnetic one has more value.

Considering the effects of the uniform magnetic field, Hosseinzadeh et al. [29] analyzed the combined natural heat exchange and thermal radiation of a hybrid nanoliquid in a porous enclosure. They reported that a higher value of the Hartmann number results in a reduction in the average Nusselt number. Brownian motion and thermophoresis effects on MHD flow of viscous nanoliquid subjected to convective surface boundary condition were examined by Hayat et al. [30]. They reported a weaker nano-additives distribution within the considered region by a higher Brownian diffusion factor. Alizadeh et al. [31] studied the magnetic field influence on thermal convection energy transport of nanosuspension inside a porous circular cylinder with an inner hot circular cylinder. The authors revealed the thermal transmission strengthening with an increase in the nano-additives concentration.

This brief review demonstrated that magnetic field effect analysis is very relevant and applicable to a variety of engineering applications. At the same time, now there are many blank spots in this research, related, for example, to non-uniform magnetic influence. It should be noted that the non-uniform magnetic impact can be found in modern heat exchangers, solar collectors, medical devices, chemical reactors, and others. Therefore, the aim of this research is a computational investigation of ferrofluid free convection in a chamber with hot semi-cylinders mounted on the bottom and left borders. The upper wall of the chamber is cold and the ferrofluid, simulated by the Buongiorno model [32], is under a non-uniform magnetic effect.

2. Materials and Methods

2.1. Problem Formulation

Figure 1 illustrates the computational domain of interest that we have used for the present study. As can be seen from this figure, two half-circles with a temperature of T_h are set on the left and bottom walls. The bottom and upper semi-cylinders have radiuses of r_1 and r_2 , respectively. The upper border has a constant low-temperature of T_c . Other parts of the cavity shell are insulated, and no-slip boundary condition is valid for all surfaces. A ferrofluid is inside the chamber. This type of nanoliquid is assumed to be viscous and

incompressible. The ferrofluid motion arising from thermogravitational energy transport is steady and laminar.

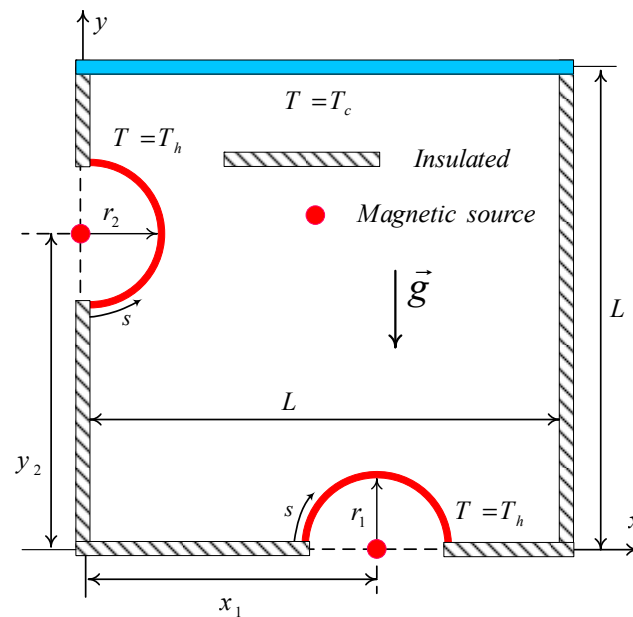


Figure 1. Configuration of the computational domain.

Here, we assume that all the parameters of the nanoliquid are constant except for the density, where its changes can be described by the Boussinesq model. The whole of the cavity domain is affected by the gravity and magnetic body forces. Two current-carrying wires as the magnetic sources are set in the center of the half-cylinders on the bottom wall in point $(x_1, 0)$ and the left wall in point $(0, y_2)$, with strengths of γ_1 and γ_2 . The magnetic fields outside half-cylinders of radiuses r_1 and r_2 are obtained as follows [15]:

$$H_1 = \frac{\gamma_1}{2\pi r_1'} \omega_{u1}, H_2 = \frac{\gamma_2}{2\pi r_2'} \omega_{u2} \tag{1}$$

where r' is the magnetic source radius and ω_u is the unit vector. Using the cartesian coordinates, we then have:

$$\begin{aligned} H_1^* &= H_{1x}^* i + H_{1y}^* j = \frac{\gamma_1}{2\pi} \frac{y}{(x-x_1)^2+y^2} i - \frac{\gamma_1}{2\pi} \frac{x-x_1}{(x-x_1)^2+y^2} j \\ H_2^* &= H_{2x}^* i + H_{2y}^* j = \frac{\gamma_2}{2\pi} \frac{y-y_2}{x^2+(y-y_2)^2} i - \frac{\gamma_2}{2\pi} \frac{x}{x^2+(y-y_2)^2} j \end{aligned} \tag{2}$$

The total vector and absolute magnitude of the magnetic force are

$$H^* = H_1^* + H_2^* = (H_{1x}^* + H_{2x}^*) i + (H_{1y}^* + H_{2y}^*) j, \quad H^* = |H^*| \tag{3}$$

Using these mentioned approaches, the governing equations describing the thermal and hydrodynamic behavior of the nanoliquid are [1,15]:

$$\nabla \cdot V = 0 \tag{4}$$

$$\begin{aligned} \rho_{nf} (V \cdot \nabla V) &= -\nabla P + \mu_{nf} \nabla \cdot \nabla V + \sigma_{nf} (V \times B) \times B + \mu_0 (M \cdot \nabla) H^* \\ &+ \rho_{f,0} g \beta_{nf} (1 - C_0) (T - T_c) j - g (\rho_p - \rho_{f,0}) (C - C_0) j \end{aligned} \tag{5}$$

where B is the magnetic induction vector with projections $B_x = \mu_0 H_x^*$ and $B_y = \mu_0 H_y^*$. ρ_{nf} , μ_{nf} , and σ_{nf} are the density, viscosity and electrical conductivity of the nanoliquid; β_{nf} is the volumetric thermal expansion of the nanoliquid; and $\rho_{f,0}$ and ρ_p are the densities of

the base fluid and nanoparticles, respectively. The magnetizable vector, M , is defined as follows:

$$M = M_x i + M_y j \mid M_x = M_y = K' H^* (T'_c - T) \tag{6}$$

where K' is a fixed value and T'_c is named the Curie temperature. The energy equation can be written as follows [15]:

$$(\rho c_p)_{nf} (V \cdot \nabla T) = k_{nf} \nabla^2 T - \mu_0 T \frac{\partial M}{\partial T} (V \cdot \nabla H^*) + \frac{J \cdot J}{\sigma_{nf}} + \Phi + \tau \left(D_B \nabla C \cdot \nabla T + \frac{D_T}{T_c} \nabla T \cdot \nabla T \right) \tag{7}$$

where $c_{p,nf}$ and k_{nf} are the specific heat capacity and thermal conductivity of the nanofluid, μ_0 is the permeability of vacuum, and D_B and D_T are the Brownian and thermophoresis coefficients of the nanofluid. $J = \sigma_{nf}(E + V \times B)$, and Φ is viscous dissipation, taking the following form:

$$\Phi = \mu_{nf} \left(2 \left(\frac{\partial u}{\partial x} \right)^2 + 2 \left(\frac{\partial v}{\partial y} \right)^2 + \left(\frac{\partial u}{\partial y} + \frac{\partial v}{\partial x} \right)^2 \right) \tag{8}$$

Using the non-homogeneous nanoliquid approach, the nanoparticles concentration equation should be added in the following form [33]:

$$(V \cdot \nabla C) = D_B \nabla^2 C + \frac{D_T}{T_c} \nabla^2 T \tag{9}$$

where C is the nanoparticle concentration. The subjected boundary conditions are:

$$\forall x, y \mid x, y \in \begin{cases} y \geq 0, (x - x_1)^2 + y^2 = r_1^2 \\ x \geq 0, x^2 + (y - y_2)^2 = r_2^2 \end{cases} \tag{10}$$

$$\Rightarrow T = T_h, u = v = 0, D_B \frac{\partial C}{\partial n} + \frac{D_T}{T_c} \frac{\partial T}{\partial n} = 0$$

It is worth noting that n refers to the direction perpendicular to the circular hot surface in the dimensional coordinate.

$$\forall x, y \mid x, y \in y = L, 0 \leq x \leq L \Rightarrow T = T_c, u = v = 0, D_B \frac{\partial C}{\partial y} + \frac{D_T}{T_c} \frac{\partial T_{nf}}{\partial y} = 0 \tag{11}$$

$$\forall x, y \mid x, y \in x = 0, \begin{cases} 0 \leq y \leq y_2 - r_2 \\ y_2 + r_2 \leq y \leq L \end{cases} \Rightarrow \frac{\partial T}{\partial x} = 0, u = v = 0, \frac{\partial C}{\partial x} = 0 \tag{12}$$

$$\forall x, y \mid x, y \in x = L, 0 \leq y \leq L \Rightarrow \frac{\partial T}{\partial x} = 0, u = v = 0, \frac{\partial C}{\partial x} = 0 \tag{13}$$

$$\forall x, y \mid x, y \in y = 0, \begin{cases} 0 \leq x \leq x_1 - r_1 \\ x_1 + r_1 \leq x \leq L \end{cases} \Rightarrow \frac{\partial T}{\partial y} = 0, u = v = 0, \frac{\partial C}{\partial y} = 0 \tag{14}$$

To non-dimensionalize the equations, the following parameters were employed:

$$X = \frac{x}{L}, Y = \frac{y}{L}, U = \frac{uL}{\alpha_{nf}}, V = \frac{vL}{\alpha_{nf}}, \theta = \frac{T - T_c}{T_h - T_c}, P = \frac{L^2 p}{\rho_{nf} \alpha_{nf}^2}, \tag{15}$$

$$H = \frac{H^*}{H_0^*}, H_X = \frac{H_x^*}{H_0^*}, H_Y = \frac{H_y^*}{H_0^*}, \phi = \frac{C}{C_0}$$

where $H_0^* = \frac{\gamma_1}{2\pi L}$. Using the above-mentioned characteristics, the governing non-dimensional equations are:

$$\frac{\partial U}{\partial X} + \frac{\partial V}{\partial Y} = 0, \tag{16}$$

$$U \frac{\partial U}{\partial X} + V \frac{\partial U}{\partial Y} = -\frac{\partial P}{\partial X} + Pr \left(\frac{\partial^2 U}{\partial X^2} + \frac{\partial^2 U}{\partial Y^2} \right) - PrHa^2 H_Y^2 U + PrHa^2 H_X H_Y V - Mn_f Pr \theta H \frac{\partial H}{\partial X} \tag{17}$$

$$U \frac{\partial V}{\partial X} + V \frac{\partial V}{\partial Y} = -\frac{\partial P}{\partial Y} + Pr \left(\frac{\partial^2 V}{\partial X^2} + \frac{\partial^2 V}{\partial Y^2} \right) - PrHa^2 H_X^2 V + PrHa^2 H_X H_Y U - Mn_f Pr \theta H \frac{\partial H}{\partial Y} + RaPr\theta + RaPrNr(1 - \phi) \tag{18}$$

$$U \frac{\partial \theta}{\partial X} + V \frac{\partial \theta}{\partial Y} = \frac{\partial^2 \theta}{\partial X^2} + \frac{\partial^2 \theta}{\partial Y^2} + EcHa^2 (UH_Y - VH_X)^2 + Nb \left(\frac{\partial \phi}{\partial X} \frac{\partial \theta}{\partial X} + \frac{\partial \phi}{\partial Y} \frac{\partial \theta}{\partial Y} \right) + Nt \left(\left(\frac{\partial \theta}{\partial X} \right)^2 + \left(\frac{\partial \theta}{\partial Y} \right)^2 \right) + Mn_f EcH(\epsilon_1 + \theta) \left(U \frac{\partial H}{\partial X} + V \frac{\partial H}{\partial Y} \right) \tag{19}$$

$$U \frac{\partial \phi}{\partial X} + V \frac{\partial \phi}{\partial Y} = \frac{1}{Le} \left(\frac{\partial^2 \phi}{\partial X^2} + \frac{\partial^2 \phi}{\partial Y^2} \right) + \frac{Nt}{Le \cdot Nb} \left(\frac{\partial^2 \theta}{\partial X^2} + \frac{\partial^2 \theta}{\partial Y^2} \right) \tag{20}$$

Here, Ra , Pr , Ha , ϵ_1 , Ec , Mn_f , Le , Nb , Nt , and Nr are the control characteristics that are the Rayleigh number, Prandtl number, Hartmann number, temperature parameter, Eckert number, magnetism number, Lewis number, Brownian motion characteristic, thermophoresis characteristic, and buoyancy ratio, respectively, which can be written as

$$Ra = \frac{g\beta_{nf}\Delta TL^3}{\nu_{nf}\alpha_{nf}}, Pr = \frac{\nu_{nf}}{\alpha_{nf}}, Ha = \mu_0 H_0^* L \sqrt{\frac{\sigma_{nf}}{\mu_{nf}}}, \epsilon_1 = \frac{T_c}{\Delta T}, Ec = \frac{\mu_{nf}\alpha_{nf}}{(\rho c_p)_{nf}\Delta TL^2}, Mn_f = \frac{\mu_0 H_0^{*2} K' \Delta TL^2}{\mu_{nf}\alpha_{nf}}, Le = \frac{\alpha_{nf}}{D_B}, Nb = \frac{\tau_{DB} C_0}{\alpha_{nf}}, Nt = \frac{\tau_{DT} \Delta T}{\alpha_{nf} T_c}, Nr = \frac{(\rho_p - \rho_{f,0}) C_0}{\rho_{nf} \beta_{nf} (1 - C_0) \Delta T} \tag{21}$$

It is assumed that the temperature of cold border is equal to the Curie temperature. Additionally, the dimensionless magnetic field projections are

$$H_X = \gamma_r (Y - Y_2) \left((Y - Y_2)^2 + X^2 \right)^{-1} + Y \left(Y^2 + (X - X_1)^2 \right)^{-1} \tag{22}$$

$$H_Y = -\gamma_r X \left(X + (Y - Y_2)^2 \right)^{-1} - (X - X_1) \left((X - X_1)^2 + Y^2 \right)^{-1} \tag{23}$$

where $\gamma_r = \gamma_2 / \gamma_1$. The non-dimensional form of the boundary conditions is:

$$\forall X, Y \mid X, Y \in \begin{cases} Y \geq 0, Y^2 + (X_1 - X)^2 = R_1^2 \\ X \geq 0, (Y_2 - Y)^2 + X^2 = R_2^2 \end{cases} \tag{24} \\ \Rightarrow U = V = 0, \theta = 1, Nb \frac{\partial \phi}{\partial N} + Nt \frac{\partial \theta}{\partial N} = 0$$

in which, N denotes to the direction perpendicular to the circular hot surface in the non-dimensional coordinate.

$$\forall X, Y \mid X, Y \in Y = 1, 0 \leq X \leq 1 \\ \Rightarrow U = V = 0, \theta = 1, Nb \frac{\partial \phi}{\partial N} + Nt \frac{\partial \theta}{\partial N} = 0 \tag{25}$$

$$\forall X, Y \mid X, Y \in X = 0, \begin{cases} 0 \leq Y \leq Y_2 - R_2 \\ Y_2 + R_2 \leq Y \leq 1 \end{cases} \\ \Rightarrow U = V = 0, \frac{\partial \theta}{\partial X} = 0, \frac{\partial \phi}{\partial X} = 0 \tag{26}$$

$$\forall X, Y \mid X, Y \in X = 1, 0 \leq Y \leq 1 \\ \Rightarrow U = V = 0, \frac{\partial \theta}{\partial X} = 0, \frac{\partial \phi}{\partial X} = 0 \tag{27}$$

$$\forall X, Y \mid X, Y \in Y = 0, \begin{cases} 0 \leq X \leq X_1 - R_1 \\ X_1 + R_1 \leq X \leq 1 \end{cases} \\ \Rightarrow \frac{\partial \theta}{\partial Y} = 0, U = V = 0, \frac{\partial \phi}{\partial Y} = 0 \tag{28}$$

For description of the heat and mass transfer intensities, the local Nusselt and Sherwood numbers at the heater surfaces were used in the following forms:

$$Nu_{local} = -\frac{\partial\theta}{\partial N} \tag{29}$$

$$Sh_{local} = -\frac{\partial\phi}{\partial N} \tag{30}$$

It is worth noting that the Nusselt number, i.e., Nu_{local} is defined as the ratio of the convective heat transfer to the conductive heat transfer. To achieve the local Nusselt number, we well know that:

$$-k_{nf}\frac{\partial T}{\partial n} = h_{nf}(T_h - T_c) \tag{31}$$

Substituting the non-dimensional parameters presented in Equation (15) in the above-mentioned equation,

$$-\frac{k_{nf}(T_h - T_c)}{L}\frac{\partial\theta}{\partial N} = h_{nf}(T_h - T_c) \Rightarrow -\frac{\partial\theta}{\partial N} = \frac{h_{nf}}{k_{nf}/L} \tag{32}$$

where $-\partial\theta/\partial N$ is defined as the Nusselt number. Obviously, according to the boundary conditions at the left and right walls, i.e., Equations (24) and (25), the Sherwood and Nusselt numbers can be converted to each other by the constant value of Nb/Nt . So, the Nusselt number is the only parameter that is examined here.

2.2. Numerical Technique

The coupled and nonlinear control equations of continuity, momentum, energy, and concentration are discretized by applying the numerical method of finite element based on the Galerkin approach along with the imposed boundary conditions. The mentioned equations are completely coupled with the use of damped Newton approach. Then, the solution of the equivalent linear algebraic equations is achieved by the Parallel Sparse Direct Solver. To expand the field variables such as $U, V, P, \theta,$ and $\phi,$ the interpolated functions listed below are employed:

$$\begin{aligned} U &\approx \sum_{e=1}^E U_e \xi_e(X, Y), V \approx \sum_{e=1}^E V_e \xi_e(X, Y), P \approx \sum_{e=1}^E P_e \xi_e(X, Y) \\ \theta &\approx \sum_{e=1}^E \theta_e \xi_e(X, Y), \phi \approx \sum_{e=1}^E \phi_e \xi_e(X, Y) \end{aligned} \tag{33}$$

Applying the Galerkin scheme, the residual equations for the above-presented field variables are:

$$\begin{aligned} R_j^1 &\approx \sum_{e=1}^E U_e \int \left[\left(\sum_{e=1}^E U_e \xi_e \right) \frac{\partial \xi_e}{\partial X} + \left(\sum_{e=1}^E V_e \xi_e \right) \frac{\partial \xi_e}{\partial Y} \right] \xi_j dXdY \\ &- \sum_{e=1}^E \int \left(\sum_{e=1}^E P_e \xi_e \right) \frac{\partial \xi_e}{\partial X} \xi_j dXdY + Pr \sum_{e=1}^E U_e \int \left[\frac{\partial \xi_e}{\partial Y} \frac{\partial \xi_j}{\partial Y} \right] dXdY \\ &+ Pr \sum_{e=1}^E U_e \int \left[\frac{\partial \xi_e}{\partial X} \frac{\partial \xi_j}{\partial X} \right] dXdY - PrHa^2 H_Y^2 \int \left(\sum_{e=1}^E U_e \xi_e \right) \xi_j dXdY \\ &+ PrHa^2 H_X H_Y \int \left(\sum_{e=1}^E V_e \xi_e \right) \xi_j dXdY - Mn_f Pr H \frac{\partial H}{\partial X} \int \left(\sum_{e=1}^E \theta_e \xi_e \right) \xi_j dXdY \end{aligned} \tag{34}$$

$$\begin{aligned}
 R_j^2 \approx & \sum_{e=1}^N V_e \int \left[\left(\sum_{e=1}^E U_e \zeta_e \right) \frac{\partial \zeta_e}{\partial X} + \left(\sum_{e=1}^E V_e \zeta_e \right) \frac{\partial \zeta_e}{\partial Y} \right] \zeta_j dXdY \\
 & - \sum_{e=1}^E \int \left(\sum_{e=1}^N P_e \zeta_e \right) \frac{\partial \zeta_j}{\partial Y} dXdY + Pr \sum_{e=1}^E V_e \int \left[\frac{\partial \zeta_e}{\partial X} \frac{\partial \zeta_j}{\partial X} \right] dXdY \\
 & + Pr \sum_{e=1}^E V_e \int \left[\frac{\partial \zeta_e}{\partial Y} \frac{\partial \zeta_j}{\partial Y} \right] dXdY - PrHa^2 H_X^2 \int \left(\sum_{e=1}^E V_e \zeta_e \right) \zeta_j dXdY \\
 & + PrHa^2 H_X H_Y \int \left(\sum_{e=1}^E U_e \zeta_e \right) \zeta_j dXdY - Mn_f Pr H \frac{\partial H}{\partial Y} \int \left(\sum_{e=1}^E \theta_e \zeta_e \right) \zeta_j dXdY \\
 & + RaPr \int \left(\sum_{e=1}^E \theta_e \zeta_e \right) \zeta_j dXdY + RaPrNr \int \left(1 - \sum_{e=1}^E \phi_e \zeta_e \right) \zeta_j dXdY
 \end{aligned} \tag{35}$$

$$R_j^3 \approx \sum_{e=1}^E U_e \int \frac{\partial \zeta_e}{\partial X} \zeta_j dXdY + \sum_{e=1}^E V_e \int \frac{\partial \zeta_e}{\partial Y} \zeta_j dXdY \tag{36}$$

$$\begin{aligned}
 R_j^4 \approx & \sum_{e=1}^E \phi_e \int \left[\left(\sum_{e=1}^E U_e \zeta_e \right) \frac{\partial \zeta_e}{\partial X} + \left(\sum_{e=1}^E V_e \zeta_e \right) \frac{\partial \zeta_e}{\partial Y} \right] \zeta_e dXdY \\
 & + \frac{1}{Le} \sum_{e=1}^E \phi_e \int \left[\frac{\partial \zeta_e}{\partial X} \frac{\partial \zeta_j}{\partial X} + \frac{\partial \zeta_e}{\partial Y} \frac{\partial \zeta_j}{\partial Y} \right] dXdY \\
 & + \frac{Nt}{LeNb} \sum_{e=1}^E \theta_e \int \left[\frac{\partial \zeta_e}{\partial X} \frac{\partial \zeta_j}{\partial X} + \frac{\partial \zeta_e}{\partial Y} \frac{\partial \zeta_j}{\partial Y} \right] dXdY
 \end{aligned} \tag{37}$$

$$\begin{aligned}
 R_j^4 \approx & \sum_{e=1}^E \theta_e \int \left[\left(\sum_{e=1}^E U_e \zeta_e \right) \frac{\partial \zeta_e}{\partial X} + \left(\sum_{e=1}^E V_e \zeta_e \right) \frac{\partial \zeta_e}{\partial Y} \right] \zeta_j dXdY \\
 & + \sum_{e=1}^E \theta_e \int \left[\frac{\partial \zeta_e}{\partial X} \frac{\partial \zeta_j}{\partial X} + \frac{\partial \zeta_e}{\partial Y} \frac{\partial \zeta_j}{\partial Y} \right] dXdY \\
 & - EcHa^2 \left[H_Y \int \left(\sum_{e=1}^E U_e \zeta_e \right) - H_X \int \left(\sum_{e=1}^E V_e \zeta_e \right) \right]^2 \zeta_j dXdY \\
 & + Mn_f EcH \left[\varepsilon_1 + \int \left(\sum_{k=1}^M \theta_e \zeta_e \right) \right] \left[\frac{\partial H}{\partial X} \int \left(\sum_{e=1}^E U_e \zeta_e \right) + \frac{\partial H}{\partial Y} \int \left(\sum_{e=1}^E V_e \zeta_e \right) \right] \\
 & + Nb \left[\int \frac{\partial}{\partial X} \left(\sum_{e=1}^E \theta_e \zeta_e \right) \zeta_i dXdY \right] \left[\int \frac{\partial}{\partial X} \left(\sum_{e=1}^E \phi_e \zeta_e \right) \zeta_i dXdY \right] \\
 & + Nb \left[\int \frac{\partial}{\partial Y} \left(\sum_{e=1}^E \theta_e \zeta_e \right) \zeta_i dXdY \right] \left[\int \frac{\partial}{\partial Y} \left(\sum_{e=1}^E \phi_e \zeta_e \right) \zeta_i dXdY \right] \\
 & + Nt \left[\int \frac{\partial}{\partial X} \left(\sum_{e=1}^E \theta_e \zeta_e \right) \zeta_i dXdY \right]^2 + Nt \left[\int \frac{\partial}{\partial Y} \left(\sum_{e=1}^E \theta_e \zeta_e \right) \zeta_i dXdY \right]^2
 \end{aligned} \tag{38}$$

Gaussian quadrature with second-order accuracy is applied to integrate the above integral residuals. Newton method using the Parallel Sparse Direct Solver (PARDISO) is also utilized to solve the residual equations, iteratively [34–36]. The more details of the method can be found in [37]. Using any numerical methods requires one to guarantee that the results are independent of the generated mesh. For following this purpose, the results have been obtained from the course to fine cells generated by a numerical approach. An unstructured mesh with the triangular cells is utilized to discretize the computational domain. Figure 2 shows that there is no important variation in the local Nusselt number for two hot cylinders 1 and 2 when the number of mesh cells meaningfully increases. Therefore, the present work utilizes the case with 2726 cells for the numerical study. It is worth noting that S is the arc length of the cylindrical heaters, as depicted in Figure 1.

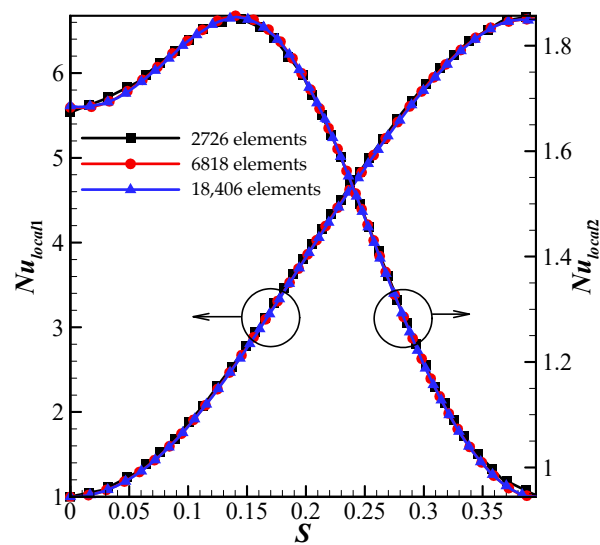


Figure 2. Mesh independence study.

2.3. Comparisons with Others

The correctness of the developed code is validated and verified by comparing the results of the current investigation and those available in [25,37,38]. In the first comparison, the temperature fields and streamlines of the current work are verified through the work of Gibanov et al. [26], as shown in Figure 3. Gibanov et al. [26] analyzed the free convection of a magnetic nanofluid flowing in a cavity partially heated from below. In the second evaluation, the numerical results of this work and the experimental results reported in [38] are compared (Figure 4). The working fluid in the enclosure is air with the Pr of 0.71 and Ra of 1.425×10^5 . The last validation, which is pictured in Figure 5, depicts the comparison between the average Nusselt number of our work and that of [39]. Kim et al. [39] studied the thermal-driven convection in a square enclosure, including a cylindrical hot heater. It worth noting that the δ parameter is the deviation of the heater from the center of the enclosure. As seen from Figures 3–5, the utilized code is valid and reliable.

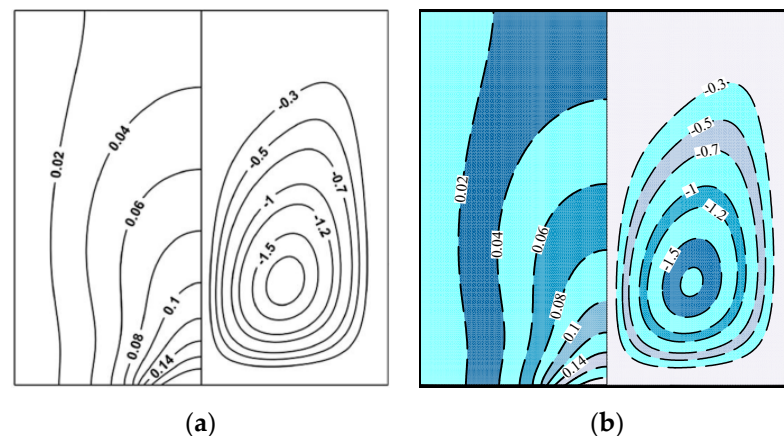


Figure 3. The motion and temperature patterns from (a) Gibanov et al. [26] and (b) current study for $Ra = 10^5$, $Ha = 10$, $Mn_f = 0.0$, $\phi = 0.04$, and $Pr = 6.2$.

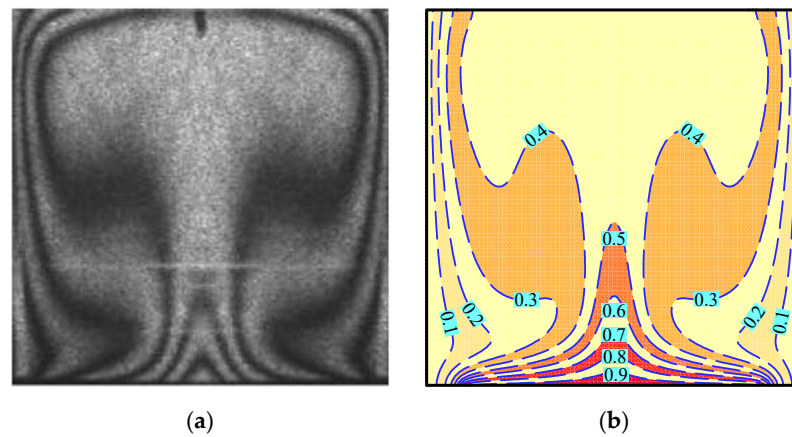


Figure 4. Isotherms from experiments of (a) Calcagni et al. [38] and (b) numerical data from the present study at $Ra = 1.425 \times 10^5$, $Ha = 0.0$, $Mn_f = 0.0$, $\phi = 0.0$, and $Pr = 0.71$.

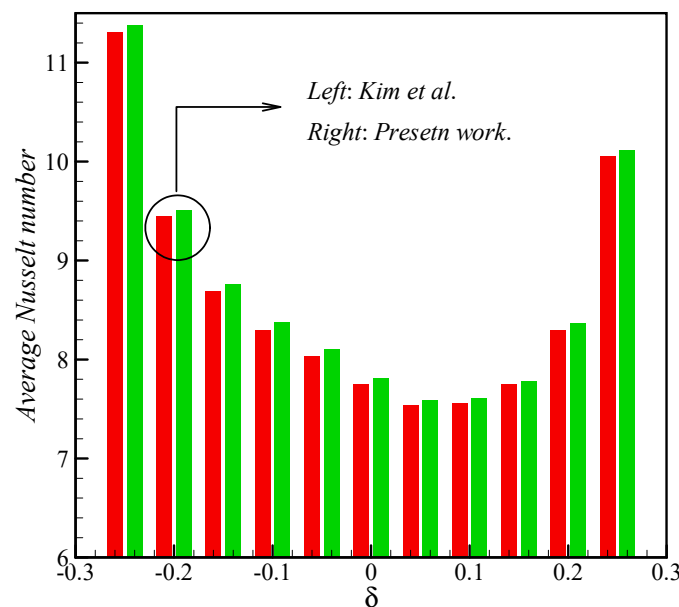


Figure 5. Average Nusselt number at the cylinder shell in comparison with numerical data of Kim et al. [39] for $Ha = 0.0$, $Mn_f = 0.0$, $\phi = 0.0$, and $Pr = 0.7$.

3. Results and Discussion

Computational analysis was performed for a wide range of key characteristics, namely, Rayleigh number ($Ra = 10^3$ and 10^5), Lewis number ($Le = 1, 10, 100$), Hartmann number ($Ha = 0, 20, 30$), magnetism number ($Mn_f = 0, 10^3, 10^4$), magnetic sources strengths ratio ($\gamma_r = 0.2, 1.0, 5.0$), buoyancy ratio ($Nr = 0.1, 0.3, 0.5$), Brownian diffusion coefficient ($Nb = 0.1, 0.5, 1.0$), and thermophoresis characteristics ($Nt = 0.1, 0.3, 0.5$). The effects of these parameters on streamlines, isotherms, isoconcentrations, and local Nusselt (or local Sherwood) numbers profiles were studied and presented in Figures 6–11.

Figure 6 shows streamlines, isotherms, and isoconcentrations within the cavity for $Mn_f = 1000$, $Ra = 10^5$, $Nb = Nt = Nr = 0.5$, $Ha = 20$, $Le = 10$ and different values of magnetic sources strengths ratio. The magnetic sources' strengths ratio reflects the ratio of the magnetic source intensity between the second source and the first one. Therefore, for $\gamma_r > 1$ one can find the dominance of left magnetic source, while for $\gamma_r < 1$ the bottom source dominates. In the case of $\gamma_r = 0.2$, only one convective clockwise vortex appears within the chamber, with upstream flows close to the left border and down-stream ones near the right vertical surface. The higher density of streamlines in the vicinity of the cylinder installed in the vertical wall compared to the lower cylinder indicates that the

flow strength next to the upper cylinder is higher. This is because the Lorentz force has a greater influence on the convection intensity in the vicinity of the lower hot surface. Simultaneously, the temperature field presents the appearance of the thermal plume over the left heater, while the bottom heater reflects the weak development of convective heat transfer. This phenomenon is attributed to the convection intensity around the cylinders, as discussed. Cooling from the upper wall defines the formation of cold descending flows near the right vertical wall that interact with hot flows close to the bottom heat source. As a result of such interaction, one can observe a reorientation of the thermal plume over this heater. The latter propagates along the bottom wall on the left side of the heater. Isoconcentrations distribution characterizes the development of areas with high and low concentrations of nano-sized solid particles. Low concentration of nanoparticles can be found near the isothermal sources, while high concentration zone is located in the right top corner. Such distribution can be described by the additional effects of thermophoresis and Brownian diffusion, which were included in the present analysis.

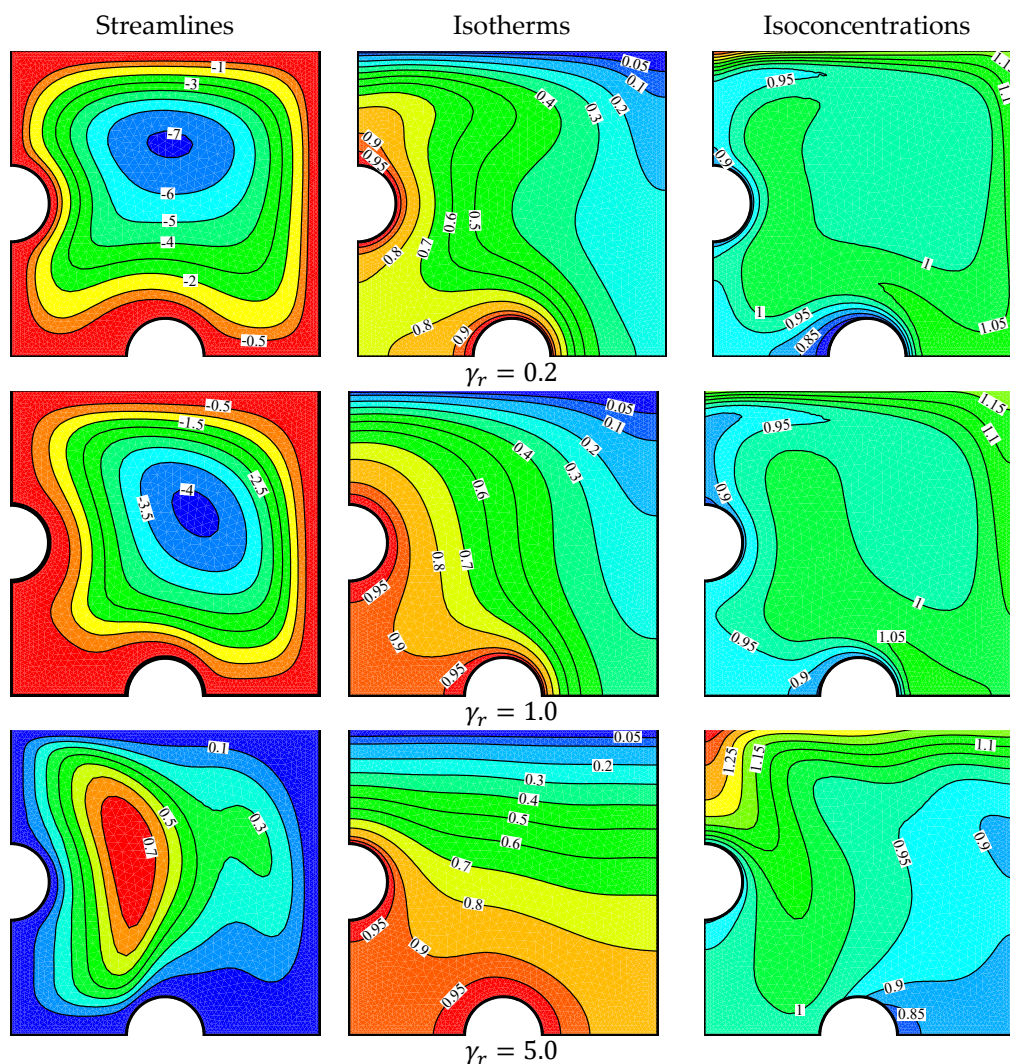


Figure 6. Nanoparticles isoconcentrations, streamlines and temperature field at different γ_r for $Mn_f = 1000$, $Ra = 10^5$, $Nb = Nt = Nr = 0.5$, $Ha = 20$, and $Le = 10$.

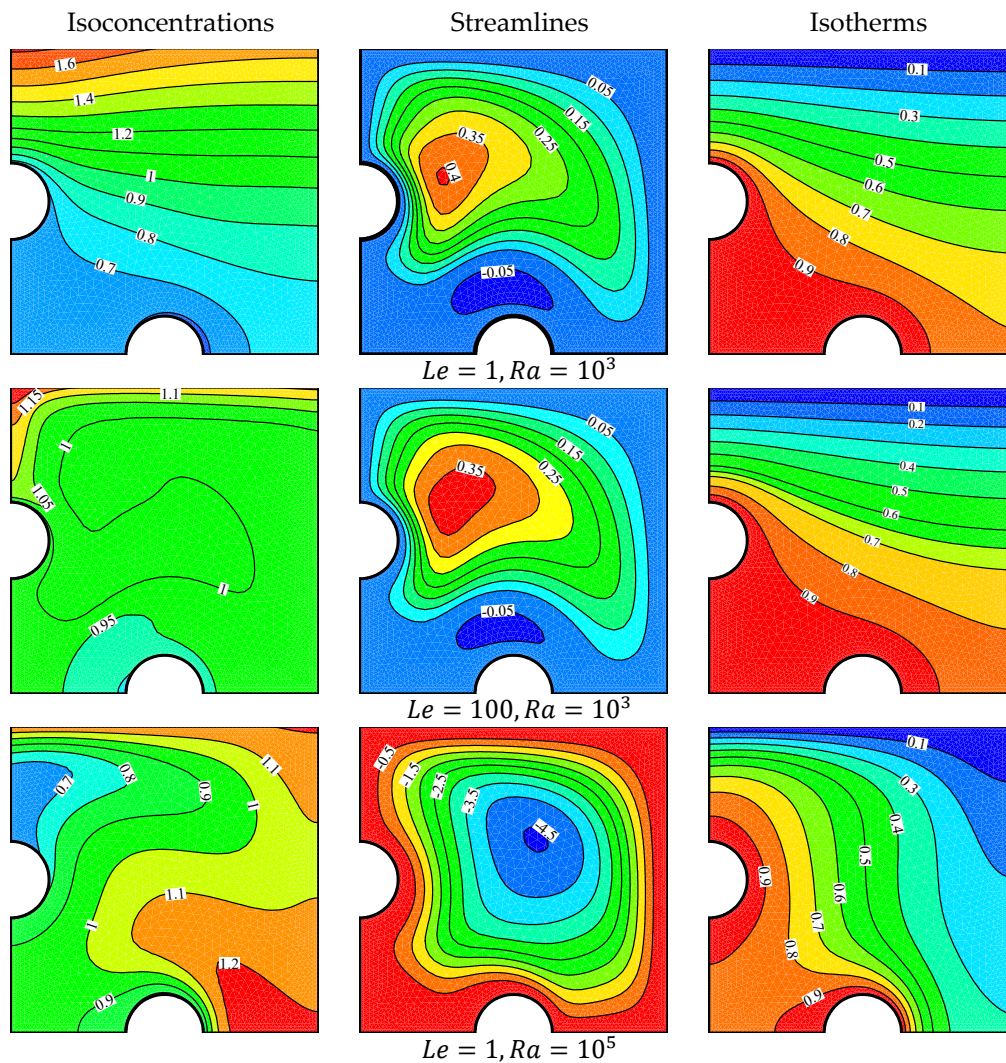


Figure 7. Isoconcentrations, streamlines and isotherms at different Lewis and Rayleigh numbers for $\gamma_r = 1$, $Mn_f = 1000$, $Nb = Nt = Nr = 0.5$, and $Ha = 20$.

The growth of $\gamma_r = 1$ results in the suppression of the convective circulation, where the convective cell core has some reorientation. Such changes are related to the suppression of the thermal plume development from the local heaters. It is well-known that intensive magnetic field suppresses the convective flow, energy, and mass transport. As a result, for case $\gamma_r = 1$, one can find a diminution of the liquid flow strength and degradation of convective energy transference. The heat diffusion dominates within the chamber, with essential heating of the zone between these two heaters. It can be seen that the mixing the nanoparticles, represented by the distortion of isoconcentrations, decreases for the case of $\gamma_r = 1$. This phenomenon is attributed to the reduction in convection intensity in the cavity.

In the case of $\gamma_r = 5$, where the upper magnetic source is dominated, the essential modification of all considered fields can be found. The main result is the domination of magnetic effect over the buoyancy force, which leads to the formation of counter-clockwise circulation of flow within the cavity. Such rearrangement characterizes an appearance of huge heat conduction area in the upper portion of the enclosure with low convective circulation intensity. Modification of the major circulation reflects the change of the nanoparticles' distribution within the chamber. The zone of maximum nano-additives concentration is the left upper corner due to the change of the heat fluxes orientation and flow direction.

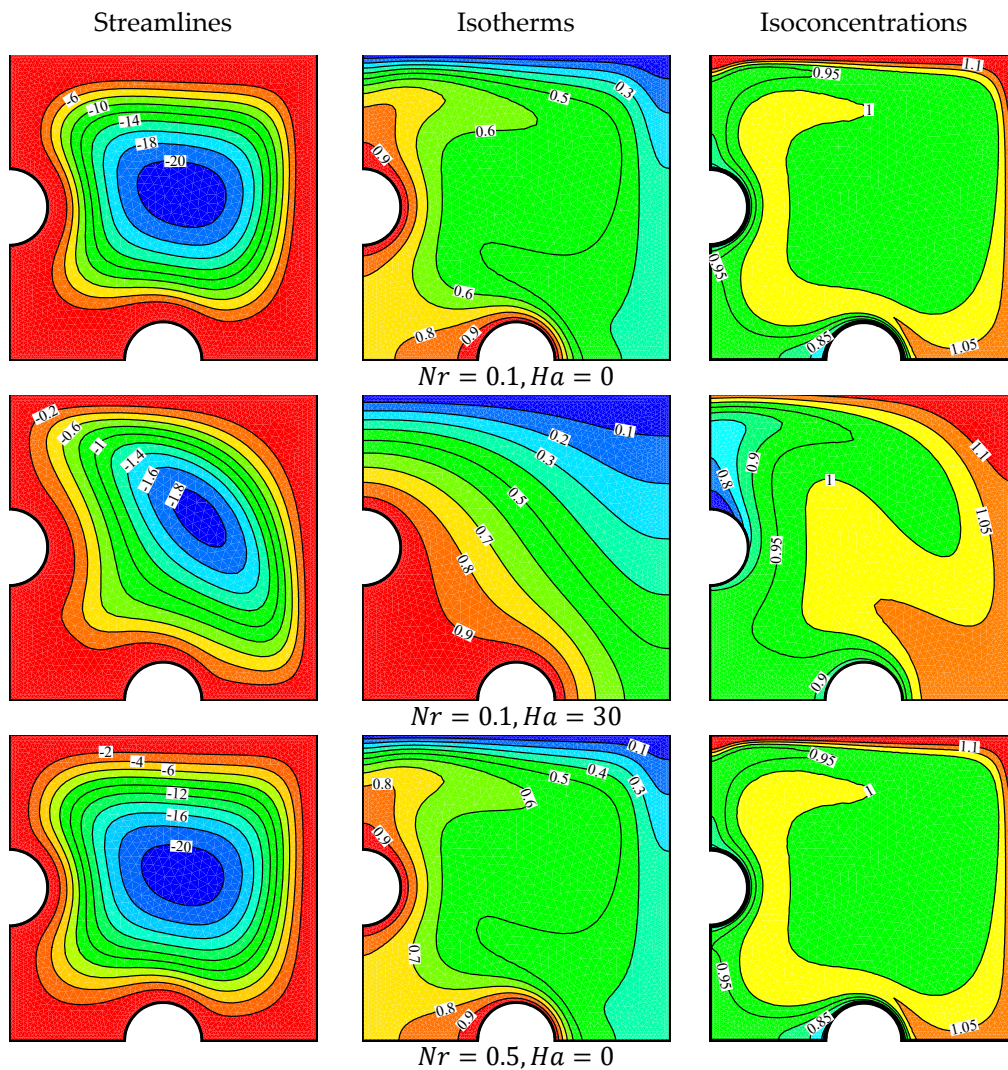


Figure 8. Isoconcentrations, streamlines and isotherms at different Nr and Ha for $\gamma_r = 1$, $Mn_f = 1000$, $Ra = 10^5$, $Nb = Nt = 0.5$, and $Le = 10$.

An impact of the Lewis and Rayleigh numbers on the distributions of the considered variables is presented in Figure 7. Changes of the Lewis number reflect the modification of the concentrations field, where an increment of Le characterizes a decrease in the concentration boundary layer thickness near the surfaces. As a result, such behavior can be found in Figure 7, namely, for $Le = 1$ one can find the development of weak diffusive mode for the propagation of the nanoparticles, while for $Le = 100$ a development of the convective mass transport can be found. Moreover, the huge value of the magnetic number reflects the degradation of convective energy transport within the chamber. Therefore, a small intensification of convective circulation with a rise of Le can be explained by the influence of the buoyancy force due to concentration gradient. As pictured, the variations of streamlines and isotherms are insignificant. It is worth noting that for $Ra = 10^3$ and $Mn_f = 1000$, a domination of the magnetic effects can be observed by the formation of a weak counter-clockwise circulation within the enclosure, while an increase in the Rayleigh number results in the domination of buoyancy-induced flow and the development of intensive clockwise vortex. The growth of Ra reflects the development of the concentration plume over the upper heater, while thermal plumes are very weak. The latter occurs owing to the strong impact of the magnetic field.

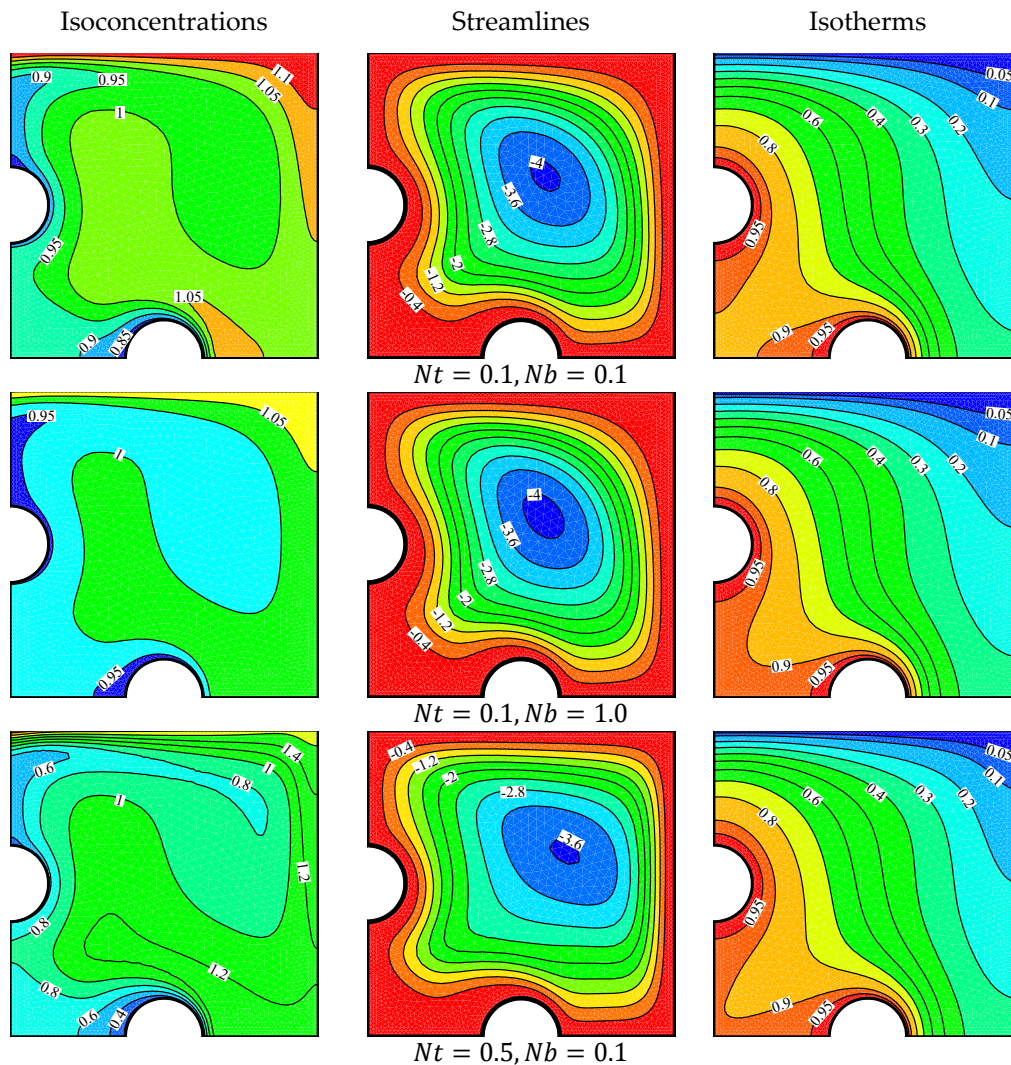


Figure 9. Nanoparticles isoconcentrations, streamlines, and temperature field at different Nt and Nb for $\gamma_r = 1$, $Mn_f = 1000$, $Ra = 10$, $Nr = 0.5$, $Ha = 20$, and $Le = 10$.

Figure 8 demonstrates the distributions of streamlines, isotherms and isoconcentrations with the Hartmann number and buoyancy ratio parameter. Addition of magnetic force with $Ha = 30$ characterizes the suppression of convective circulation, mass and energy transports within the chamber, and the domination of the diffusive regime for the heat and mass transport processes. It is interesting to note that Lorentz force that is described by the Hartmann number has a hydrodynamic nature, and the modification of convective circulation with Ha has an indirect impact on the temperature and concentration fields. In fact, the Lorentz force resists buoyancy, leading to a decrease in the thermal and mass mixings.

The buoyancy ratio parameter (Nr) shows the ratio of the buoyancy caused by the difference between the density of the nanoparticles and the base fluid of the buoyancy resulting from the temperature gradients. Rise of the buoyancy ratio parameter for the case of $Ha = 0$ characterizes an insignificant modification of the considered variables.

Influences of the Brownian diffusion (Nb) and thermophoresis characteristics (Nt) on isoconcentrations, streamlines, and isotherms are shown in Figure 9. A rise of Nb leads to significant variation in the nanoparticles' concentration field, while streamlines and isotherms are changed weakly. With the growth of the Brownian diffusion parameter, we have a weak propagation of nanoparticles within the enclosure with essential heating of the stagnation zone between the local heaters. Simultaneously, a rise of the thermophoresis characteristic, i.e., Nt , reflects an essential modification of isoconcentration distribution, an attenuation of convective circulation, and less heating of the region between the local heaters.

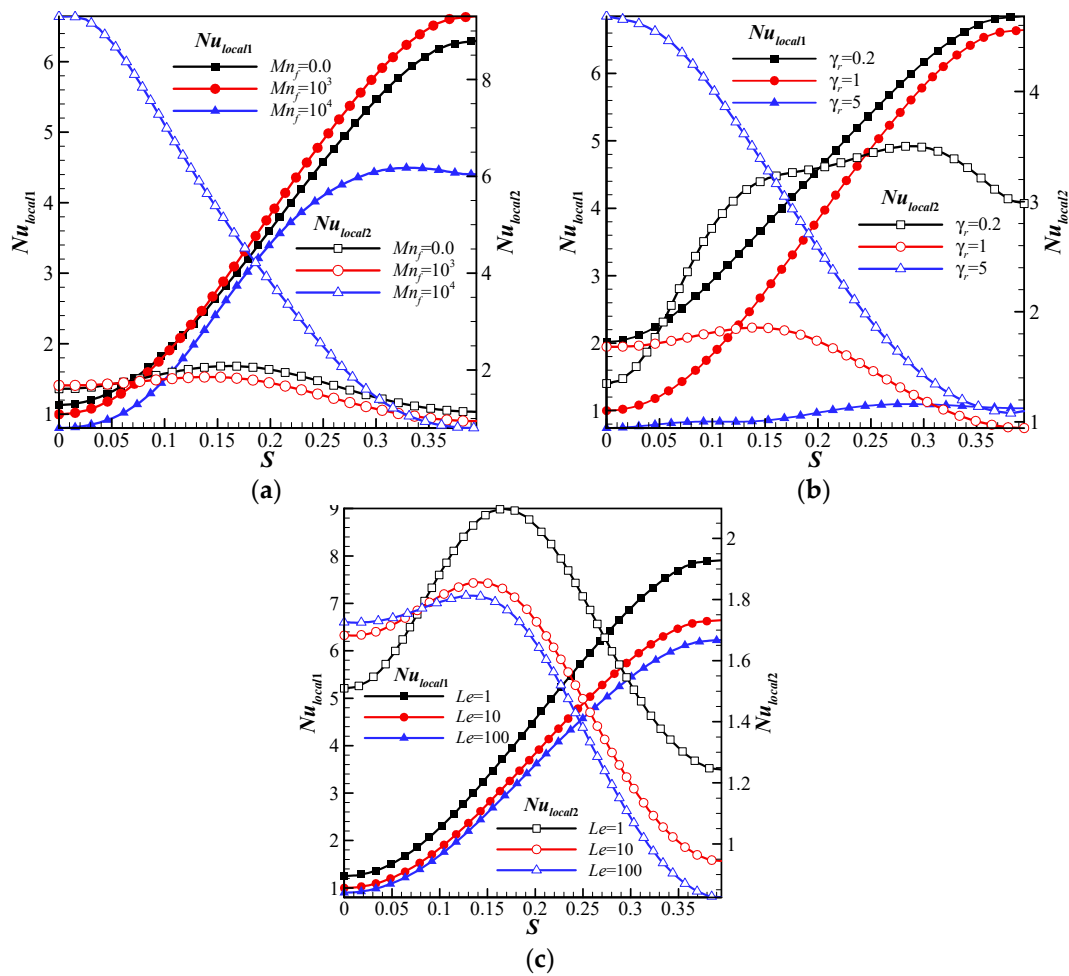


Figure 10. Profiles of local Nusselt number for variation of (a) Mn_f , (b) γ_r , and (c) Le , along two semi-cylinders for $Ra = 10^5$, $Nb = Nt = Nr = 0.5$, and $Ha = 20$.

It is possible to explain the behavior of the local Nusselt (or Sherwood) numbers along the surfaces of the isothermal heaters by taking into account these distributions. It is found that for all values of Mn_f , the maximum Nu_{local2} occurred at the lowest point of the cylinder and it continuously decreased along the surface of the cylinder. As pictured in the isotherms' contours (for the studied cases), the nanofluid moving upward along the surface of the cylinder heats up. Therefore, the temperature gradients between the cylinder hot surface and the adjacent nanofluid decline, leading to decrease in the Nu_{local1} . However, Nu_{local1} experiences its highest value where S is maximum. This is also because the nanofluid located in the vicinity of the S maximum has the lowest temperature.

The magnetic number has a nonlinear influence on the temperature gradient, namely, for growth of Mn_f between 0 and 1000 one can find an increment of Nu_{local1} and a reduction of Nu_{local2} , while for an increase in Mn_f between 1000 and 10,000 we have the opposite effect, namely, Nu_{local1} decreases but Nu_{local2} increases, as shown in Figure 10a. Such behavior can be explained by strengthening of the magnetic field effects that lead to rearrangement of the flow structures and temperature field within the chamber. Figure 10b demonstrates the curves of local Nusselt numbers along the heaters surfaces for various magnitudes of γ_r . First of all, according to the governing contours, the nature of Nu_{local1} illustrates a rise of the thermal gradient from the left lower corner till the right bottom edge that is caused by the interaction between the cold and hot flows from the right part and the formation of the stagnant zone between the heaters. The growth of γ_r reflects a reduction of Nu_{local1} that illustrates the formation of magnetic influence opposing the buoyancy impact. In more detail, as shown in Figure 6, an increase in the γ_r leads to an increase in the thermal boundary layer thickness, meaning a decrease in the temperature gradients.

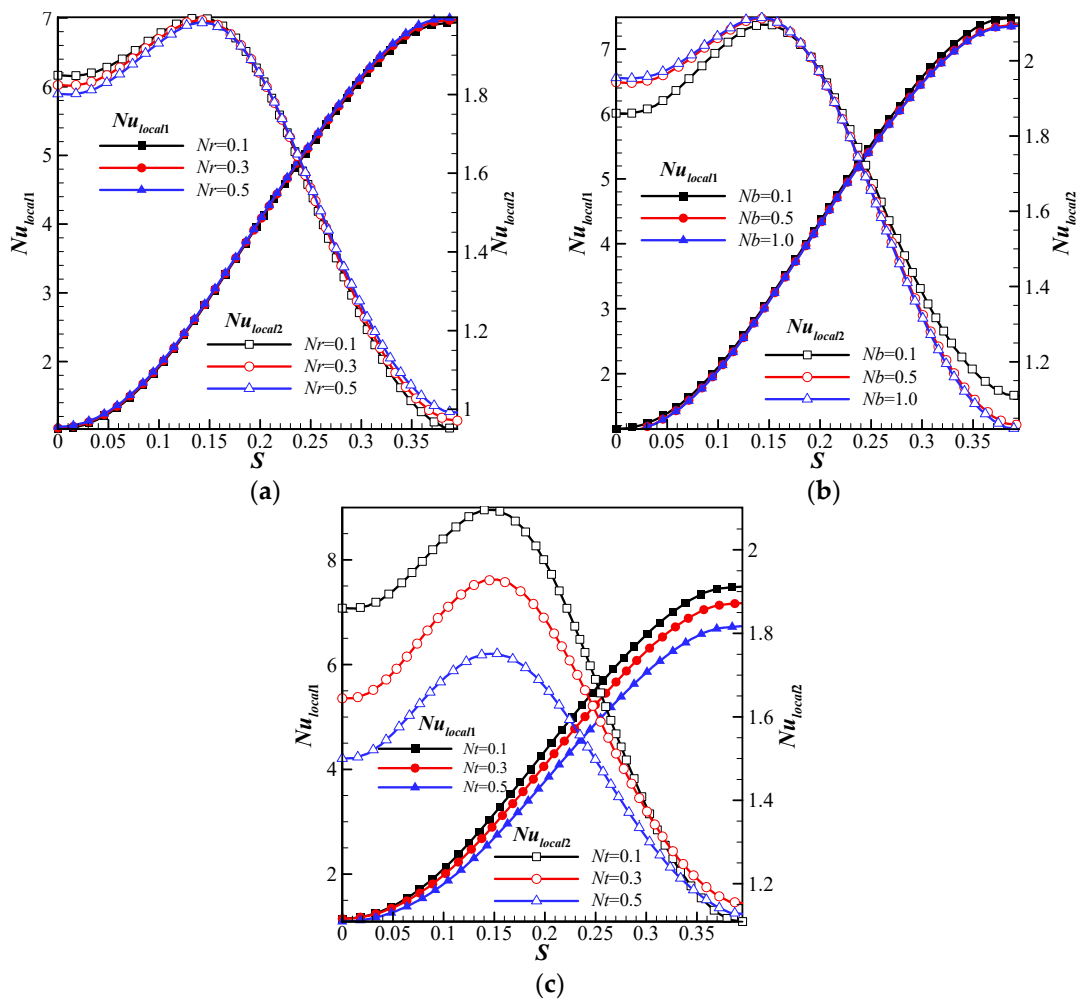


Figure 11. Profiles of local Nusselt number for variation of (a) Nr , (b) Nb , and (c) Nt along two semi-cylinders for $\gamma_r = 1.0$, $Mn_f = 1000$, $Ra = 10^5$, $Ha = 20$, and $Le = 10$.

At the same time, the behavior of Nu_{local2} is more interesting, namely, a rise of γ_r between 1 and 5 leads to the growth of heat removal from the upper heater, while for $\gamma_r \in (0.2, 1)$, the Nusselt number profile reflects the domination of thermal plume over this heater, where the temperature gradient is less than that under the heater. As a result, the typical profile of Nu_{local2} characterizes a diminution of the temperature gradient along the heater surface from the bottom point till the upper one. In other words, based upon the isotherms presented in Figure 6, the thickness of the thermal boundary layer increases when reaching γ_r from 0.2 to 1, meaning a decrease in the temperature gradients. However, an inverse trend is found for the thermal boundary layer when γ_r increases from 1 to 5. The behavior of the local Nusselt numbers with the Lewis number can be found in Figure 10c. The profiles of the local Nusselt numbers are typical for the considered sources, and augmentation of Le causes a diminution of Nu_{local1} and Nu_{local2} . Such variation is a result of the diminution of the thickness of the concentration boundary layer with a rise of the concentration gradient that leads to a degradation of the buoyancy force. Regarding Equations (24) and (25), it is worth noting that the value of mass transfer represented by the Sherwood number is exactly equal to the Nusselt number.

Figure 11a demonstrates the profiles of the local Nusselt numbers for various magnitudes of the buoyancy ratio. As was mentioned above, the growth of Nr does not have an essential influence on the temperature gradient. One can find only a weak increase in these heat transfer parameters. The mentioned weak effect of the Brownian diffusion parameter is confirmed by low variation of the local Nusselt number presented in Figure 11b, while the rise of the thermophoresis parameter (Nt) characterizes a reduction of the temperature

gradient along the surfaces of the heater. Hence, the heat transfer rates along the hot surfaces decrease with an increase in the thermophoresis parameter, as depicted in Figure 11c. Moreover, it is found that the Nu_{local2} increases with increasing S and then decreases until it attains its minimum value. According to the isotherms depicted in Figures 8 and 9, the thermal boundary layer thickness firstly decreases and then increases when moving along the hot cylinder surface.

4. Conclusions

This study deals with computational analysis of magnetic nanoliquid behavior within a chamber with two local heaters possessing two magnetic sources in the presence of Brownian diffusion and thermophoresis impacts. The investigation has been performed for a wide range of control characteristics. The obtained results have revealed that

- The rise of the magnetic sources strengths ratio illustrates an increase in the upper magnetic source power that reflects an increment of the thermal diffusive zone in the upper part of the cavity. As a result, the Nu_{local} along the bottom hot element decreases, but along the upper one increases;
- An increment of Le characterizes a decrease of the heat transfer rate.
- The rise of the thermophoresis parameter reflects a reduction of Nu_{local} , while major modifications can be found only in distributions of nanoparticles;
- The influence of the Brownian diffusion characteristic and buoyancy ratio is non-significant.
- An increase in Mn_f from 0 to 1000 leads to an increment of Nu_{local1} and a reduction of Nu_{local2} . However, the opposite effects can be observed while increasing Mn_f from 1000 to 10,000.
- An increase in the Nr is associated with an insignificant increase in the Nusselt number.

Author Contributions: Conceptualization, N.B.K., M.S. and S.A.M.M.; methodology, M.S., A.S.A., A.M.; software, A.M., A.S.A. and S.A.M.M.; validation, M.S., A.S.A. and S.A.M.M.; formal analysis, N.B.K., A.M.; investigation, N.B.K., M.S. and S.A.M.M.; resources, A.S.A. and A.M.; data curation, A.S.A., A.M. and S.A.M.M.; writing—original draft preparation, N.B.K. and M.S.; writing—review and editing, N.B.K., M.S. and S.A.M.M.; supervision, M.S. and S.A.M.M. All authors have read and agreed to the published version of the manuscript.

Funding: This research received no external funding.

Institutional Review Board Statement: Not applicable.

Informed Consent Statement: Not applicable.

Data Availability Statement: Data are contained within the article.

Acknowledgments: This work of Mikhail A. Sheremet was supported by the Tomsk State University Development Programme (Priority-2030).

Conflicts of Interest: The authors declare no conflict of interest.

References

1. Punith Gowda, R.J.; Naveen Kumar, R.; Jyothi, A.M.; Prasannakumara, B.C.; Sarris, I.E. Impact of binary chemical reaction and activation energy on heat and mass transfer of marangoni driven boundary layer flow of a non-Newtonian nanofluid. *Processes* **2021**, *9*, 702. [\[CrossRef\]](#)
2. Izadi, M.; Shahmardan, M.; Behzadmehr, A. Richardson number ratio effect on laminar mixed convection of a nanofluid flow in an annulus. *Int. J. Comput. Methods Eng. Sci. Mech.* **2013**, *14*, 304–316. [\[CrossRef\]](#)
3. Selimefendigil, F.; Öztop, H.F. Control of natural convection in a CNT-water nanofluid filled 3D cavity by using an inner T-shaped obstacle and thermoelectric cooler. *Int. J. Mech. Sci.* **2020**, *169*, 105104. [\[CrossRef\]](#)
4. Arshad, A.; Jabbar, M.; Sardari, P.T.; Bashir, M.A.; Faraji, H.; Yan, Y. Transient simulation of finned heat sinks embedded with PCM for electronics cooling. *Therm. Sci. Eng. Prog.* **2020**, *18*, 100520. [\[CrossRef\]](#)
5. Alsabery, A.I.; Armaghani, T.; Chamkha, A.J.; Hashim, I. Two-phase nanofluid model and magnetic field effects on mixed convection in a lid-driven cavity containing heated triangular wall. *Alex. Eng. J.* **2020**, *59*, 129–148. [\[CrossRef\]](#)
6. Li, Z.; Shahsavari, A.; Al-Rashed, A.A.; Talebizadehsardari, P. Effect of porous medium and nanoparticles presences in a counter-current triple-tube composite porous/nano-PCM system. *Appl. Therm. Eng.* **2020**, *167*, 114777. [\[CrossRef\]](#)

7. Alsabery, A.I.; Mohebbi, R.; Chamkha, A.J.; Hashim, I. Effect of local thermal non-equilibrium model on natural convection in a nanofluid-filled wavy-walled porous cavity containing inner solid cylinder. *Chem. Eng. Sci.* **2019**, *201*, 247–263. [[CrossRef](#)]
8. Sardari, P.T.; Giddings, D.; Grant, D.; Gillott, M.; Walker, G.S. Discharge of a composite metal foam/phase change material to air heat exchanger for a domestic thermal storage unit. *Renew. Energy* **2020**, *148*, 987–1001. [[CrossRef](#)]
9. Hayat, T.; Aziz, A.; Muhammad, T.; Alsaedi, A. Numerical treatment for Darcy–Forchheimer flow of nanofluid due to a rotating disk with convective heat and mass conditions. *Int. J. Numer. Methods Heat Fluid Flow* **2018**, *28*, 2531–2550. [[CrossRef](#)]
10. Hayat, T.; Aziz, A.; Muhammad, T.; Alsaedi, A. Numerical simulation for three-dimensional flow of Carreau nanofluid over a nonlinear stretching surface with convective heat and mass conditions. *J. Braz. Soc. Mech. Sci. Eng.* **2019**, *41*, 55. [[CrossRef](#)]
11. Garmroodi, M.D.; Ahmadpour, A.; Talati, F. MHD mixed convection of nanofluids in the presence of multiple rotating cylinders in different configurations: A two-phase numerical study. *Int. J. Mech. Sci.* **2019**, *150*, 247–264. [[CrossRef](#)]
12. Selimefendigil, F.; Özttop, H.F. Magnetic field effects on the forced convection of CuO-water nanofluid flow in a channel with circular cylinders and thermal predictions using ANFIS. *Int. J. Mech. Sci.* **2018**, *146*, 9–24. [[CrossRef](#)]
13. Shafiq, A.; Hammouch, Z.; Sindhu, T. Bioconvective MHD flow of tangent hyperbolic nanofluid with newtonian heating. *Int. J. Mech. Sci.* **2017**, *133*, 759–766. [[CrossRef](#)]
14. Nayak, M. MHD 3D flow and heat transfer analysis of nanofluid by shrinking surface inspired by thermal radiation and viscous dissipation. *Int. J. Mech. Sci.* **2017**, *124*, 185–193. [[CrossRef](#)]
15. Izadi, M.; Mohebbi, R.; Delouei, A.A.; Sajjadi, H. Natural convection of a magnetizable hybrid nanofluid inside a porous enclosure subjected to two variable magnetic fields. *Int. J. Mech. Sci.* **2019**, *151*, 154–169. [[CrossRef](#)]
16. Selimefendigil, F.; Özttop, H.F. Fluid-solid interaction of elastic-step type corrugation effects on the mixed convection of nanofluid in a vented cavity with magnetic field. *Int. J. Mech. Sci.* **2019**, *152*, 185–197. [[CrossRef](#)]
17. Hayat, T.; Riaz, R.; Aziz, A.; Alsaedi, A. Analysis of entropy generation for MHD flow of third grade nanofluid over a nonlinear stretching surface embedded in a porous medium. *Phys. Scr.* **2019**, *94*, 125703. [[CrossRef](#)]
18. Sheikholeslami, M.; Shehzad, S.; Li, Z. Nanofluid heat transfer intensification in a permeable channel due to magnetic field using lattice Boltzmann method. *Phys. B Condens. Matter* **2018**, *542*, 51–58. [[CrossRef](#)]
19. Malmir-Chegini, Y.; Amanifard, N. Heat transfer enhancement inside semi-insulated horizontal pipe by controlling the secondary flow of oil-based ferro-fluid in the presence of non-uniform magnetic field: A general correlation for the Nusselt number. *Appl. Therm. Eng.* **2019**, *159*, 113839. [[CrossRef](#)]
20. Gui, N.G.J.; Stanley, C.; Nguyen, N.-T.; Rosengarten, G. Ferrofluids for heat transfer enhancement under an external magnetic field. *Int. J. Heat Mass Transf.* **2018**, *123*, 110–121.
21. Bezaatpour, M.; Goharkhah, M. Effect of magnetic field on the hydrodynamic and heat transfer of magnetite ferrofluid flow in a porous fin heat sink. *J. Magn. Magn. Mater.* **2019**, *476*, 506–515. [[CrossRef](#)]
22. Zhou, J.; Gu, G.; Meng, X.; Shao, C. Effect of alternating gradient magnetic field on heat transfer enhancement of magnetoreological fluid flowing through microchannel. *Appl. Therm. Eng.* **2019**, *150*, 1116–1125. [[CrossRef](#)]
23. Asadi, A.; Nezhad, A.H.; Sarhaddi, F.; Keykha, T. Laminar ferrofluid heat transfer in presence of non-uniform magnetic field in a channel with sinusoidal wall: A numerical study. *J. Magn. Magn. Mater.* **2019**, *471*, 56–63. [[CrossRef](#)]
24. Zonouzi, S.A.; Khodabandeh, R.; Safarzadeh, H.; Aminfar, H.; Trushkina, Y.; Mohammadpourfard, M.; Ghanbarpour, M.; Alvarez, G.S. Experimental investigation of the flow and heat transfer of magnetic nanofluid in a vertical tube in the presence of magnetic quadrupole field. *Exp. Therm. Fluid Sci.* **2018**, *91*, 155–165. [[CrossRef](#)]
25. Fadaei, F.; Dehkordi, A.M.; Shahrokhi, M.; Abbasi, Z. Convective-heat transfer of magnetic-sensitive nanofluids in the presence of rotating magnetic field. *Appl. Therm. Eng.* **2017**, *116*, 329–343. [[CrossRef](#)]
26. Gibanov, N.S.; Sheremet, M.A.; Ozttop, H.F.; Nusier, O.K. Convective heat transfer of ferrofluid in a lid-driven cavity with a heat-conducting solid backward step under the effect of a variable magnetic field. *Numer. Heat Transf. Part A Appl.* **2017**, *72*, 54–67. [[CrossRef](#)]
27. Selimefendigil, F.; Ozttop, H.F.; Sheremet, M.A.; Abu-Hamdeh, N. Forced convection of Fe₃O₄-water nanofluid in a bifurcating channel under the effect of variable magnetic field. *Energies* **2019**, *12*, 666. [[CrossRef](#)]
28. Mehryan, S.; Izadi, M.; Chamkha, A.J.; Sheremet, M.A. Natural convection and entropy generation of a ferrofluid in a square enclosure under the effect of a horizontal periodic magnetic field. *J. Mol. Liq.* **2018**, *263*, 510–525. [[CrossRef](#)]
29. Hosseinzadeh, K.; Roghani, S.; Mogharrebi, A.; Asadi, A.; Ganji, D. Optimization of hybrid nanoparticles with mixture fluid flow in an octagonal porous medium by effect of radiation and magnetic field. *J. Therm. Anal. Calorim.* **2021**, *143*, 1413–1424. [[CrossRef](#)]
30. Hayat, T.; Aziz, A.; Muhammad, T.; Alsaedi, A. On magnetohydrodynamic three-dimensional flow of nanofluid over a convectively heated nonlinear stretching surface. *Int. J. Heat Mass Transf.* **2016**, *100*, 566–572. [[CrossRef](#)]
31. Dogonchi, A.; Sheremet, M.A.; Ganji, D.; Pop, I. Free convection of copper–water nanofluid in a porous gap between hot rectangular cylinder and cold circular cylinder under the effect of inclined magnetic field. *J. Therm. Anal. Calorim.* **2019**, *135*, 1171–1184. [[CrossRef](#)]
32. Buongiorno, J. Convective transport in nanofluids. *J. Heat Transf.* **2006**, *128*, 240–250. [[CrossRef](#)]
33. Tahmasebi, A.; Mahdavi, M.; Ghalambaz, M. Local thermal nonequilibrium conjugate natural convection heat transfer of nanofluids in a cavity partially filled with porous media using Buongiorno’s model. *Numer. Heat Transf. Part A Appl.* **2018**, *73*, 254–276. [[CrossRef](#)]

34. Schenk, O.; Gärtner, K. Solving unsymmetric sparse systems of linear equations with PARDISO. *Future Gener. Comput. Syst.* **2004**, *20*, 475–487. [[CrossRef](#)]
35. Wriggers, P. *Nonlinear Finite Element Methods*; Springer Science & Business Media: Berlin/Heidelberg, Germany, 2008.
36. Verbosio, F.; De Coninck, A.; Kourounis, D.; Schenk, O. Enhancing the scalability of selected inversion factorization algorithms in genomic prediction. *J. Comput. Sci.* **2017**, *22*, 99–108. [[CrossRef](#)]
37. Reddy, J.N.; Gartling, D.K. *The Finite Element Method in Heat Transfer and Fluid Dynamics*; CRC Press: Boca Raton, FL, USA, 2010.
38. Calcagni, B.; Marsili, F.; Paroncini, M. Natural convective heat transfer in square enclosures heated from below. *Appl. Therm. Eng.* **2005**, *25*, 2522–2531. [[CrossRef](#)]
39. Kim, B.; Lee, D.; Ha, M.; Yoon, H. A numerical study of natural convection in a square enclosure with a circular cylinder at different vertical locations. *Int. J. Heat Mass Transf.* **2008**, *51*, 1888–1906. [[CrossRef](#)]